

# Numerical simulations of inertial microbubble collapse at a gel–water interface with finite elasticity and phase change

By M. Carcana Barbosa<sup>†¶</sup>, M. Rodriguez Jr.<sup>†¶</sup> AND J. Yang<sup>‡</sup>

Microcavitation near soft biological material can lead to finite material deformations and potentially damage. During microcavitation, the microbubble undergoes rapid oscillations and phase change occurs between the water vapor and surrounding liquid water at the microbubble surface. Previous studies of an inertial bubble collapse near compliant material interfaces were limited to shock-induced collapse such that phase change could be neglected, and considered only the bubble collapse in the liquid (water) phase near the soft material. Thus, the fluid-structure interaction of microcavitation in or near soft materials undergoing finite deformations in the presence of phase change remains unknown. We extend the multi-component flow code (MFC), a fully Eulerian finite-volume solver, to account for material hyperelasticity with the reference map technique (RMT). The algorithm employs a six-equation model for the stiffened gas equation of state (EoS) with an infinite relaxation approach to account for phase change. We consider problem setups of a microbubble composed of water vapor and noncondensable gas inertially collapsing near or in a soft hyperelastic material and compare with experiments. The numerical simulations match the shear strain field experimental observations of a laser-induced bubble near or in a 3% polyacrylamide, 0.2% bisacrylamide hydrogel.

---

## 1. Introduction

In high-strain rate events such as ballistic blasts or explosions, the body is subject to traumatic injury (Kim *et al.* 2021). Local and transient pressure changes from the impacts (energy deposition) lead to high strains and potentially shocks that propagate throughout the soft material. Shocks are discontinuities in pressure, density, and temperature. Although not fully understood, the compliance and compressibility of soft materials contribute to the nonlinearity of the dynamics (Dollet *et al.* 2019). The rapid transient pressure drop in a liquid below its saturated vapor pressure at a given temperature may result in inertial cavitation. Cavitation microbubbles are nucleated and inertially oscillate in volume (with strain rates  $> 10^3$  1/s) until mechanical dissipation slows the dynamics toward mechanical equilibrium (Estrada *et al.* 2018). These dynamics can be reproduced experimentally via laser- and acoustically generated microbubbles in soft materials (e.g., hydrogels) to gain insight into the high-strain rate material response. However, to understand the underlying material response in high-strain, nonsymmetric, heterogeneous environments, time- and space-resolved spatial data is necessary.

<sup>†</sup> Center for Fluid Mechanics, School of Engineering, Brown University

<sup>¶</sup> These authors equally contributed to this work.

<sup>‡</sup> Department of Aerospace Engineering and Engineering Mechanics, The University of Texas at Austin

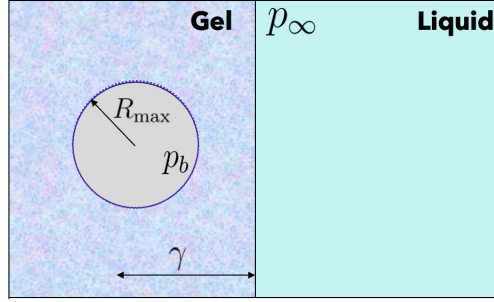


FIGURE 1. Problem setup of a water vapor and noncondensable gas-filled microbubble initialized in gel near a gel–liquid interface at fixed nondimensional standoff distance  $\gamma$ .

Numerical simulations complement experimental efforts by accessing spatiotemporal scales and spatial data not typically available in experiments. Monolithic Eulerian interface-capturing approaches solving the compressible Navier–Stokes equations in an  $N$ -material framework have favorable attributes over Lagrangian or arbitrary Lagrangian–Eulerian methods due to algorithmic simplicity and discrete conservation (Rodriguez & Johnsen 2019; Jain *et al.* 2023). Finite-volume, interface- and shock-capturing numerical simulation approaches have been developed over the past decade for accurate computation of compressible multiphase flows (Jain *et al.* 2023), including bubble dynamics (Coralic & Colonius 2014; Shams *et al.* 2023). However, computing finite deformations in the Eulerian framework is particularly challenging when incorporating material elasticity. Two Eulerian approaches are available in the literature: (i) Godunov approaches (Ndanou *et al.* 2017; Shams *et al.* 2023) and (ii) the reference map technique (RMT) (Valkov *et al.* 2015; Jain *et al.* 2019). Due to its applicability to a wide range of hyperelastic constitutive models and simple implementation, we consider the RMT in this work. The RMT utilizes the reference map of the spatial configuration to the reference configuration and can model incompressible hyperelastic solids (Jain *et al.* 2019). At the elastic material interface, the rapid bubble oscillations show nonequilibrium thermodynamics such as phase change. To account for phase change, we use the six-equation multiphase model of Pelanti & Shyue (2019). The model considers pressure, thermal, and chemical disequilibrium at an interface of the same substance (e.g., liquid water and water vapor) and assumes thermodynamic equilibrium is achieved infinitely fast.

The objective of this work is to understand soft material deformation due to a microbubble collapse, including phase-change dynamics, near a gel–water interface. We model the hydrogel as a hyperelastic, neo-Hookean material and implement the RMT in the multi-component flow code (MFC). The MFC (Radhakrishnan *et al.* 2024) is a GPU-accelerated, finite-volume conservative solver. The remainder of this proceeding is organized as follows. The problem setup and governing equations are presented in Section 2. Numerical methods are presented in Section 3. In Section 4, we present results comparing the bubble morphology and shear strain fields with digital image correlation (DIC) results from laser-induced cavitation experiments of the same initial geometry. We conclude with our observations in Section 5.

## 2. Problem setup and governing equations

### 2.1. Problem setup

We investigate laser-induced inertial cavitation near a gel–water interface at the maximum microbubble radius. In the experiments, a laser pulse deposits energy into the gel or liquid to generate an optically focused, single cavitation bubble at various stand-off distances from an embedded specked gel–water interface. Using the spatiotemporal adaptive quadtree mesh DIC technique (McGhee *et al.* 2023; Yang *et al.* 2022), we extract high-resolution spatiotemporal shear strain spatial fields. Figure 1 shows one of the problem setups for the numerical simulations, in which a microbubble is placed in a gel near an initially straight liquid–gel interface. An initially spherical bubble at its maximum radius,  $R_{\max}$ , is composed of water vapor and a noncondensable gas, and placed at a normalized standoff distance,  $\gamma = \Delta x/R_{\max}$ , from the gel–liquid interface, where  $\Delta x$  is the standoff distance from the interface. Matching experiments, we consider two numerical simulations at the maximum microbubble radius of  $\gamma = 2.17$  or  $-1.39$ . A negative (positive)  $\gamma$  indicates the bubble is initialized in the gel (liquid). The maximum experimentally observed radii,  $R_{\max} = 244.8 \mu\text{m}$  and  $R_{\max} = 230.4 \mu\text{m}$  for bubbles initialized in the gel and water, respectively, are used in the numerical simulations. In the experiments, the initial condition is the laser-induced generated bubble, which is out of mechanical equilibrium with its surroundings. However, since the shear modulus is low relative to collapse inertia, we consider numerical simulations initially in mechanical equilibrium. That is, the elastic material field is not prestressed at  $R_{\max}$ . In the simulations, the surrounding liquid and gel have an initial pressure,  $p_{\infty} = 5 \text{ MPa}$ , consistent with prior studies of an inertial microbubble collapse (Rodriguez *et al.* 2022). The bubble has an initial pressure of saturated water vapor,  $p_b = 3550 \text{ Pa}$ , at temperature  $T = 300 \text{ K}$ .

The experimental and numerical results are nondimensionalized by their respective theoretical Rayleigh collapse time,  $t_c = 0.9125R_{\max}\sqrt{\rho/\Delta p}$ , where  $\rho$  is the surrounding material density and  $\Delta p = p_{\infty} - p_b$ . For the experiments, we assume an atmospheric surrounding pressure and  $p_b = 3550 \text{ Pa}$  for the initial bubble pressure. Thus, the theoretical Rayleigh collapse times are  $t_c = 22.6 \mu\text{s}$  and  $t_c = 21.3 \mu\text{s}$  for the bubble initialized in the liquid and gel, respectively. For the simulations, the collapse times are  $t_c = 3.71 \mu\text{s}$  and  $t_c = 3.49 \mu\text{s}$  for the bubble initialized in the liquid and gel, respectively. The numerical simulation collapse times are shorter than the experimental values due to the higher initial surrounding material pressure driving the collapse. The gel consists of 3% polyacrylamide and 0.2% bisacrylamide and has a dynamic shear modulus of  $G = 0.57 \text{ kPa}$ .

### 2.2. Governing equations

#### 2.2.1. Equations of motion

The MFC solves the six-equation  $N$ -component multiphase model of Pelanti & Shyue (2019) with phase change between the first and second phases,

$$\partial_t \mathbf{q} + \nabla \cdot \mathbf{F}(\mathbf{q}) + \mathbf{h}(\mathbf{q})\nabla \cdot \mathbf{u} = \mathbf{r}_{\mu}(\mathbf{q}) + \mathbf{r}_{\theta}(\mathbf{q}) + \mathbf{r}_{\nu}(\mathbf{q}), \quad (2.1)$$

where  $\mathbf{q}$  is the state vector,  $\mathbf{F}$  is the flux tensor,  $\mathbf{h}$  is the nonconservative term, and the right-hand-side source terms involve the pressure (mechanical), thermal, and chemical

disequilibrium, respectively. The terms are defined as

$$\mathbf{q} = \begin{bmatrix} \alpha_1 \\ \alpha_2 \\ \vdots \\ \alpha_N \\ \alpha_1 \rho_1 \\ \vdots \\ \alpha_N \rho_N \\ \rho \mathbf{u} \\ \alpha_1 \mathcal{E}_1 \\ \vdots \\ \alpha_N \mathcal{E}_N \end{bmatrix}, \quad \mathbf{F} = \begin{bmatrix} \alpha_1 \mathbf{u} \\ \alpha_2 \mathbf{u} \\ \vdots \\ \alpha_N \mathbf{u} \\ \alpha_1 \rho_1 \mathbf{u} \\ \vdots \\ \alpha_N \rho_N \mathbf{u} \\ \rho \mathbf{u} \otimes \mathbf{u} + \sum_{k=1}^N \alpha_k p_k \mathbf{I} - \boldsymbol{\sigma}^{\text{dev}} \\ \alpha_1 \mathcal{E}_1 \mathbf{u} \\ \vdots \\ \alpha_N \mathcal{E}_N \mathbf{u} \end{bmatrix}, \quad \mathbf{h} = \begin{bmatrix} -\alpha_1 \\ -\alpha_2 \\ \vdots \\ -\alpha_N \\ 0 \\ \vdots \\ 0 \\ 0 \\ \alpha_1 p_1 \\ \vdots \\ \alpha_N p_N \end{bmatrix}, \quad (2.2)$$

$$\mathbf{r}_\mu = \begin{bmatrix} \sum_{j=1}^N \mathcal{P}_{1j} \\ \sum_{j=1}^N \mathcal{P}_{2j} \\ \vdots \\ \sum_{j=1}^N \mathcal{P}_{Nj} \\ 0 \\ 0 \\ \vdots \\ 0 \\ 0 \\ -\sum_{j=1}^N p_{1j} \mathcal{P}_{1j} \\ -\sum_{j=1}^N p_{2j} \mathcal{P}_{2j} \\ \vdots \\ -\sum_{j=1}^N p_{Nj} \mathcal{P}_{Nj} \end{bmatrix}, \quad \mathbf{r}_\theta = \begin{bmatrix} 0 \\ 0 \\ \vdots \\ 0 \\ 0 \\ 0 \\ \vdots \\ 0 \\ 0 \\ \sum_{j=1}^N \mathcal{Q}_{1j} \\ \sum_{j=1}^N \mathcal{Q}_{2j} \\ \vdots \\ \sum_{j=1}^N \mathcal{Q}_{Nj} \end{bmatrix}, \quad \mathbf{r}_\nu = \begin{bmatrix} 0 \\ 0 \\ \vdots \\ 0 \\ \mathcal{M} \\ -\mathcal{M} \\ \vdots \\ 0 \\ 0 \\ g_I \mathcal{M} \\ -g_I \mathcal{M} \\ \vdots \\ 0 \end{bmatrix}, \quad (2.3)$$

where  $\rho_k$ ,  $\alpha_k$ ,  $p_k$ , and  $\mathcal{E}_k$  are the phase  $k$  density, volume fraction, pressure, and specific internal energy per unit volume, respectively, and  $\mathbf{I}$  is the identity tensor. The mixture relations are  $\sum_k \alpha_k = 1$  and  $\sum_k \rho_k \alpha_k = \rho$ , where  $\rho$  is the mixture density. The mixture internal (hydrostatic) energy per unit volume is  $\mathcal{E} = \sum_k \alpha_k \mathcal{E}_k$  and is related to thermodynamic quantities through the EoS. We consider isotropic materials and follow the same energy decomposition as Ndanou *et al.* (2017). The total energy (per unit volume)  $E$  is the sum of internal (hydrostatic), kinetic, and elastic contributions:  $E = \mathcal{E} + (1/2)\rho \mathbf{u} \cdot \mathbf{u} + \rho e^e$ , where  $e^e$  is the elastic energy per unit mass. Elastic energy is defined by a constitutive relation that describes the change of energy due to mechanical deformations and defines the Cauchy stress tensor. To maintain numerical stability (Schmidmayer *et al.* 2020), the total energy is numerically conserved by solving an additional equation,  $\partial_t E + \nabla \cdot ((E + p)\mathbf{u} - \boldsymbol{\sigma}^{\text{dev}} \cdot \mathbf{u}) = 0$ . The Cauchy stress tensor is decomposed into isotropic and deviatoric components:  $\boldsymbol{\sigma} = \boldsymbol{\sigma}^{\text{iso}} + \boldsymbol{\sigma}^{\text{dev}}$ . All of these terms have viscous and elastic contributions. Elasticity dominates during the inertial collapse of the bubble (Estrada *et al.* 2018); thus, we neglect viscous effects. The isotropic term consists of pressure ( $\boldsymbol{\sigma}^{\text{iso}} = -p\mathbf{I}$ ), and is incorporated into Eq. (2.1) for each phase. The deviatoric stress contribution is defined with a constitutive relation. The terms  $\mathcal{P}_{kj}$

TABLE 1. Constants in the stiffened gas EoS for water (LeMetayer *et al.* 2004).

Water phase	$n$	$B$ [MPa]	$q$ [kJ/kg]	$\eta$ [kJ/(kg K)]	$c_v$ [J/(kg K)]	$c_p$ [J/(kg K)]
Liquid	2.35	$10^3$	-1167	0	1816	4267
Vapor	1.43	0	2030	-23.4	1040	1487

and  $\mathcal{Q}_{kj}$  represent the volume transfer (pressure disequilibrium) and heat transfer, respectively, between phases  $k$  and  $j$ . The term  $\mathcal{M}$  is the mass transfer between phases 1 and 2, the liquid and vapor phases, respectively. These transfer terms are defined as  $\mathcal{P}_{kj} = \mu_{kj}(p_k - p_j)$ ,  $\mathcal{Q}_{kj} = \theta_{kj}(T_j - T_k)$ , and  $\mathcal{M} = \nu(g_2 - g_1)$ , where  $T_k$  denotes the temperature and  $g_k$  the Gibbs free energy (chemical potential) of phase  $k$ . The parameters  $\mu_{jk}$ ,  $\theta_{jk}$ , and  $\nu$  have no physical interpretation and are assumed to be infinite near the interface and zero elsewhere; that is,

$$\mu_{jk}, \theta_{jk} = \begin{cases} \infty & \text{if } \epsilon \leq \alpha_k \leq 1 - \epsilon, \\ 0 & \text{otherwise,} \end{cases}, \quad \nu = \begin{cases} \infty & \text{if } \epsilon \leq \alpha_k \leq 1 - \epsilon \text{ and } T_{\text{liq}} > T_{\text{sat}}, \\ 0 & \text{otherwise,} \end{cases} \quad (2.4)$$

where  $\epsilon$  defines the liquid–vapor interface, set to  $\epsilon = 10^{-6}$  (Saurel *et al.* 2008).

### 2.2.2. Equation of state

The stiffened gas EoS of LeMetayer *et al.* (2004) is used to relate the mixture internal energy to pressure and temperature as

$$\mathcal{E} = \sum_{k=1}^N \alpha_k \mathcal{E}_k = p \sum_{k=1}^N \frac{\alpha_k}{n_k - 1} + \sum_{k=1}^N \alpha_k \frac{n_k B_k}{n_k - 1} + \sum_{k=1}^N \rho_k \alpha_k q_k, \quad (2.5a)$$

$$= T \sum_{k=1}^N \rho_k \alpha_k c_{v,k} + \sum_{k=1}^N \alpha_k B_k + \sum_{k=1}^N \rho_k \alpha_k q_k, \quad (2.5b)$$

respectively, where  $T$  is the temperature and  $q_k$ ,  $n_k$ ,  $B_k$ , and  $c_{v,k}$  are phase  $k$  material properties. The phasic material properties are obtained empirically to produce the experimentally observed propagation speeds in the water gas and liquid phase for a temperature range  $T = 300$ – $600$  K. The phasic Gibbs free energy, used to model phase transition and equilibrium, is defined as

$$g_k = (n_k c_{v,k} - \eta_k) T_k + q_k - c_{v,k} T_k \ln \left( \frac{T_k^{n_k}}{(p_k + B_k)^{n_k - 1}} \right), \quad (2.6)$$

where  $\eta_k$  is a phase  $k$  material parameter. Table 1 lists the phenomenological constants for water vapor and liquid water.

### 2.2.3. Hyperelasticity

The gradient of the reference map is the inverse of the deformation gradient (Jain *et al.* 2019):  $\mathbf{F} = (\nabla \boldsymbol{\xi})^{-1}$ . An evolution equation for the reference map is combined with the conservation of mass equation to obtain a conservative form:  $\partial_t(\rho \boldsymbol{\xi}) + \nabla \cdot (\rho \mathbf{u} \otimes \boldsymbol{\xi}) = \mathbf{0}$ . The equation is combined with the system of equations in Eq. (2.1) and solved during the hyperbolic step of the solver. The left Cauchy–Green deformation tensor is then calculated as  $\mathbf{b} = \mathbf{F} \mathbf{F}^\top$ . For compressible neo-Hookean materials, the strain energy density function may be written in terms of the left Cauchy–Green deformation tensor (Bonet & Wood

(1997)),  $\psi(\mathbf{b}) = (\lambda/2)(\ln(J))^2 - G \ln J + (G/2)(I_{\mathbf{b}} - 3)$ , where  $J$  is the determinant of the deformation gradient tensor,  $\lambda$  is a Lamé parameter,  $G$  is the shear modulus, and  $I_{\mathbf{b}}$  is the first invariant of the left Cauchy–Green deformation tensor. We additively decompose the motion and strain energy function into dilatational (volume-changing) and isochoric (volume-preserving):  $\psi(\mathbf{b}) = \psi^{\text{vol}}(J) + \tilde{\psi}(\tilde{\mathbf{b}})$ , respectively (Chaves 2013). The volumetric term is associated with the internal (hydrostatic) energy and an EoS relating pressure, temperature, and density. The isochoric term is the deviatoric part of the Cauchy stress tensor for a compressible neo-Hookean model,  $\boldsymbol{\sigma}^{\text{dev}} = (G/J)(\mathbf{b} - (1/3)\text{tr}(\mathbf{b})\mathbf{I})$ , and closes Eq. (2.1). The mixture shear modulus is weighed by the volume fraction as  $G = \sum_k \alpha^{(k)} G^{(k)}$ .

### 3. Numerical methods

Equation (2.1) is solved using the Strang splitting approach (Strang 1968) involving two solvers: hyperbolic and relaxation. For the hyperbolic step, a Harten Lax-van Leer and contact (HLLC) approximate Riemann solver and a third-order, total variation diminishing Runge–Kutta algorithm upwind the solution. Fifth-order, accurately weighted, essentially nonoscillatory schemes are used for spatial reconstruction (Coralic & Colonius 2014). The MFC uses a shock- and interface-capturing numerical method that is high-order accurate and discretely conservative. The reference map is initialized in mechanical equilibrium as the coordinate position at each grid point,  $\boldsymbol{\xi} = \mathbf{x}$ . The gradient of the reference map  $\nabla \boldsymbol{\xi}$  is computed using a fourth-order central finite-difference scheme. The deformation gradient tensor,  $\mathbf{F}$ , is obtained by inverting the gradient of the reference map. The left Cauchy–Green strain tensor,  $\mathbf{b}$ , and the deviatoric contribution to the Cauchy stress tensor,  $\boldsymbol{\sigma}^{\text{dev}}$ , are then computed with the deformation gradient tensor. For the relaxation step, we follow the relaxation procedure of Pelanti & Shyue (2019) in which the first two phases (i.e., liquid water and water vapor) can undergo phase change. Phase change is activated if either the liquid temperature is above or the water vapor below the saturation temperature. The remaining phases are relaxed to pressure and thermal equilibrium. The experiment uses low-polymer-concentration hydrogel such that it is mostly composed of water. Thus, the phase change is assumed to take place between the liquid water in the bubble surroundings and the water vapor in the bubble.

### 4. Results

Figures 2 and 3 show the shear strain ( $e_{xy}$ ) in the soft material (rainbow) contours for the numerical simulations (left column) and experiments (right column) for  $\gamma = 2.17$  and  $-1.39$ , respectively. The shear strain contour levels and magnitudes match between the numerical simulations and experiments. For the numerical simulations, pressure is in grayscale and the orange isosurface represents the bubble surface at the volume fraction of the surrounding material,  $\alpha_m = 0.5$ . The orange dashed line is the bubble initial location and size. Shortly after reaching the minimum volume, a shock, originating from the bubble surface at minimum volume, propagates radially outward and through the nearby elastic material for positive  $\gamma$ . For both  $\gamma$  cases, the bubble collapse morphology is not spherical in the numerical simulations due to the fluid-structure interactions with the surroundings. While phase change took place between the water vapor in the bubble and the surroundings (data not shown), the inertia of the collapse dominates the collapse dynamics.

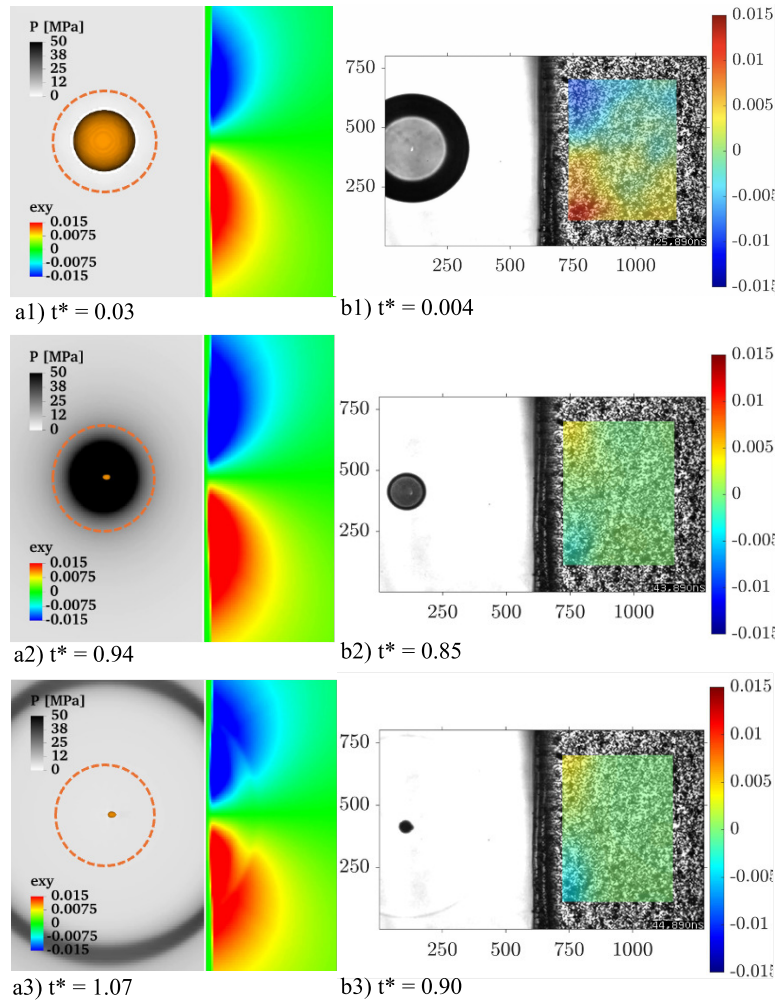


FIGURE 2. (a1 - a3) Simulation and (b1 - b3) experimental shear strain contours in the  $xy$  plane (rainbow scale) of a bubble initialized in liquid of a gel–water interface at  $\gamma = 2.17$ . For the numerical simulation contours, pressure contours in the liquid water are shown in grayscale and the orange isosurfaces denote the bubble surface at  $\alpha_\ell = 0.5$ . Times are nondimensionalized by their respective theoretical Rayleigh collapse time.

#### 4.1. Bubble initialized in liquid near a gel–water interface, $\gamma = 2.17$

For both the experiment and numerical simulation, the collapse is spherical due to the uniform pressure in the surroundings. The bubble reaches minimum volume at the theoretical Rayleigh collapse time. At minimum volume, the transfer of kinetic energy from the liquid to internal energy of the bubble gases arrests the liquid motion at the bubble surface. However, the surrounding fluid continues to converge on the bubble and becomes compressed (Figure 2(a2)). The liquid pressure near the bubble rapidly increases at the minimum volume and generates a shock that propagates radially outward (Figure 2(a3)) into the neighboring soft material. There is minimal partial reflection of the shock at the material interface due to the liquid water and soft material having similar acoustic impedances. During the collapse, two nodal shear strain structures form, with the highest-

and lowest-strain-magnitude values near the material interface (Figure 2(*a3,b1*)). In the experiment, the strain magnitudes decrease as the bubble returns to mechanical equilibrium. As the bubble reaches mechanical equilibrium in the experiments, the shear strains dissipate more quickly than in the numerical simulations. An inversion in polarity is observed in the shear strain in Figure 2(*b2,b3*) when the bubble radius decreases in size past the mechanical equilibrium. In the numerical simulations, two shear strain nodes form as the bubble collapses and entrains the material surroundings, including the soft, elastic material. Despite not matching the initial condition of the experiments, the maximum shear strains and shapes of the simulations qualitatively match those of the experiments. Moreover, the shock waves in Figure 2(*a3,b3*) are approximately at similar locations.

#### 4.2. Bubble initialized in gel near a gel–water interface, $\gamma = -1.39$

For the case of the bubble collapsing in the gel, the collapse is more asymmetrical than the  $\gamma = 2.17$  case. The bubble reaches its minimum volume at the theoretical collapse time. Soon after the bubble begins to collapse in both the experiments and simulations, four shear strain nodes form in the soft material near the surface of the bubble (Figure 3(*a1,b1*)). The shear strain nodes continue to grow during the bubble collapse (Figure 3(*a2,a3*)). In the experimental results, the maximum shear strain in these four nodes is observed at the maximum radius (Figure 3(*b1*)) due to the out-of-equilibrium condition at the maximum bubble radius. In Figure 3(*b3*), the bubble decreases in size past the mechanical equilibrium radius due to the collapse inertia, and the shear strain nodes change polarity. However, in the numerical simulations, the mechanical equilibrium radius is much smaller and not reached during the collapse. Thus, the polarity of the shear strain is retained (Figure 3(*a3*)). The shear strain magnitudes between the simulation and experiment do not match due to the higher inertia in liquid pressure driving the collapse in the numerical simulations. Relative to the  $\gamma = 2.17$  case, the shear strains are stresses more than 10 times larger for the bubble in the gel than for the bubble initialized in the water.

## 5. Conclusions

We conducted Eulerian numerical simulations of hyperelastic solids and phase change using MFC to study inertial microbubble cavitation near a gel–water material interface. We implemented a hyperelastic formulation for a neo-Hookean material using the RMT. Two cases of an inertially collapsing bubble near a gel–water interface are considered: a bubble initialized in (i) water at  $\gamma = 2.17$  and (ii) gel at  $\gamma = -1.39$ . While phase change took place in the simulations, the high inertial pressure dominated the collapse dynamics such that its effect was not significant. The bubble morphology is spherical during the collapse. Additionally, collapse times match their theoretical values for both simulations and experiments. The resulting shear strains in the nearby elastic material are due to the bubble entraining the surrounding material during the collapse. Between the two experiments, a microbubble initialized in a soft material can generate shear strains more than 10 times larger than when initialized in water. For both standoff distances, the elastic material shear strain magnitudes and spatial shapes of the numerical simulations match the DIC shear strain experiments before reaching the mechanical equilibrium radius. In future work, we will consider the bubble growth phase where phase change is more significant and account for the displaced gel–water interface when the bubble reaches its maximum volume.

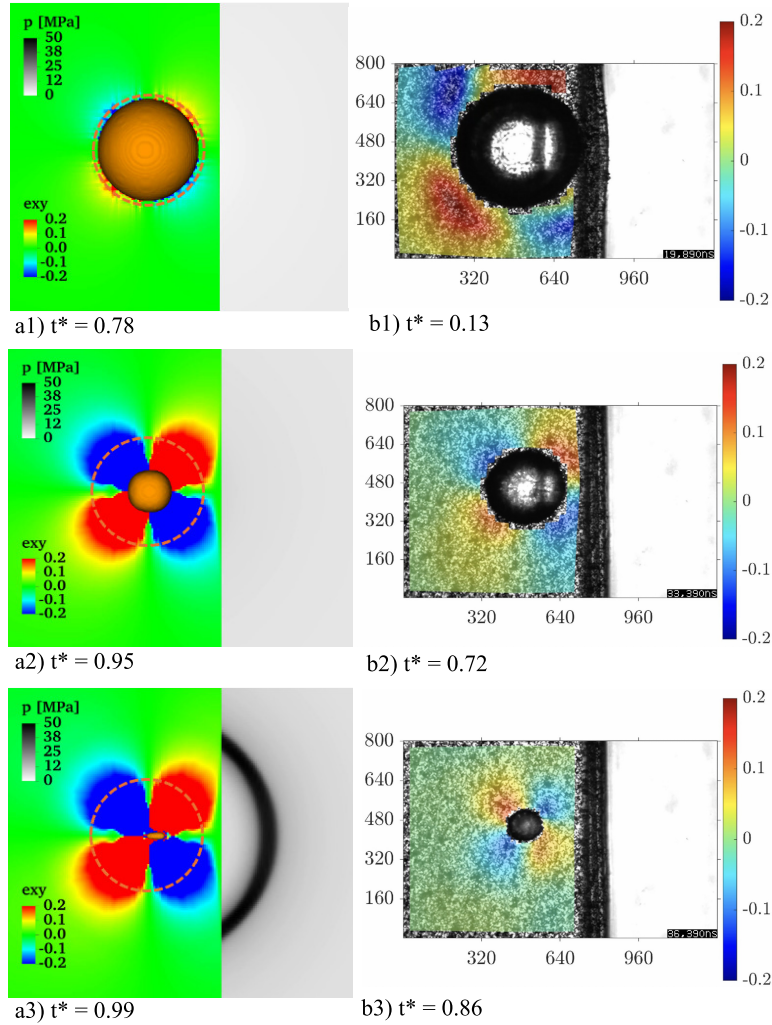


FIGURE 3. (a1 - a3) Simulation and (b1 - b3) experimental shear strain contours in the  $xy$  plane (rainbow scale) of a bubble initialized in the gel of a gel-water interface at  $\gamma = -1.39$ . For the numerical simulation, pressure contours in liquid water are shown in grayscale and the orange isosurface denotes the bubble surface at  $\alpha_{\text{gel}} = 0.5$ . Times are nondimensionalized by their respective theoretical Rayleigh collapse time.

#### Acknowledgments

This work is supported by the US Office of Naval Research (grant FA9550-23-1-0485) under Dr. Timothy Bentley and by the US National Science Foundation (grants 2232427 and 2232428), and used computing resources through allocation MCH220010 from the Advanced Cyberinfrastructure Coordination Ecosystem: Services & Support (ACCESS) program, which is supported by National Science Foundation (grants 2138259, 2138286, 2138307, 2137603, and 2138296). J.Y. acknowledges the start-up fund from the University of Texas at Austin and the Haythornthwaite Foundation for the Research Initiation Grant awarded by Applied Mechanics Division of the American Society of Mechanical Engineers.

## REFERENCES

- BONET, J. & WOOD, R. 1997 *Nonlinear Continuum Mechanics for Finite Element Analysis*. Cambridge University Press.
- CHAVES, E. 2013 *Notes on Continuum Mechanics*. Springer.
- CORALIC, V. & COLONIUS, T. 2014 Finite-volume WENO scheme for viscous compressible multicomponent flows. *J. Comput. Phys.* **274**, 95–121.
- DOLLET, B., MARMOTTANT, P. & GARBIN, V. 2019 Bubble dynamics in soft and biological matter. *Annu. Rev. Fluid Mech.* **51**, 331–355.
- ESTRADA, J., BARAJAS, C., HENANN, D., JOHNSEN, E. & FRANCK, C. 2018 High strain-rate soft material characterization via inertial cavitation. *J. Mech. Phys. Sol.* **112**, 291–317.
- JAIN, S., KAMRIN, K. & MANI, A. 2019 A conservative and non-dissipative Eulerian formulation for the simulation of soft solids in fluids. *J. Comput. Phys.* **399**, 108922.
- JAIN, S., ADLER, M., WEST, J., MANI, A., MOIN, P. & LELE, S. 2023 Assessment of diffuse-interface methods for compressible multiphase fluid flows and elastic-plastic deformation in solids. *J. Comput. Phys.* **475**, 111866.
- KIM, C., CHOI, W., NG, Y. & KANG, W. 2021 Mechanically induced cavitation in biological systems. *Life* **11**, 546.
- LE METAYER, O., MASSONI, J. & SAUREL, R. 2004 Elaboration des lois d'état d'un liquide et de sa vapeur pour les modèles d'écoulements diphasiques. Elaborating equations of state of a liquid and its vapor for two-phase flow models; *Int. J. Therm. Sci.* **43**, 265–276 .
- MCGHEE, A., YANG, J., BREMMER, E. C., XU, Z., CRAMER, H. C., ESTRADA, E. B., HENANN, D. L. & FRANCK, C. 2023 High-speed, full-field deformation measurements near inertial microcavitation bubbles inside viscoelastic hydrogels. *Exp. Mech.* **63**, 63–78.
- NDANOU, S., FAVRIE, N. & GAVRILYUK, S. 2017 The piston problem in hyperelasticity with the stored energy in separable form. *Math. Mech. Solids.* **22**, 101–113.
- PELANTI, M. & SHYUE, K.-M. 2019 A numerical model for multiphase liquid–vapor–gas flows with interfaces and cavitation, *Int. J. Multiphas. Flow.* **113**, 208–230.
- RADHAKRISHNAN, A., LE BERRE, H., WILFONG, B., SPRATT, J., RODRIGUEZ, M., COLONIUS, T. & BRYNGELSON, S. 2024 Method for scalable and performant GPU-accelerated simulation of multiphase compressible flow. *Comput. Phys. Commun.* **302**, 109238.
- RODRIGUEZ, M., BEIG, S. A., BARBIER, C. N. & JOHNSEN, E. 2022 Dynamics of an inertially collapsing gas bubble between two parallel, rigid walls. *J. Fluid Mech.* **946**, A43.
- RODRIGUEZ, M. & JOHNSEN, E. 2019 A high-order accurate five-equations compressible multiphase approach for viscoelastic fluids and solids with relaxation and elasticity. *J. Comput. Phys.* **379**, 70–90.
- SAUREL, R., PETITPAS, F. & ABGRALL, R. 2008 Modeling phase transition in metastable liquids. Application to flashing and cavitating Flows. *J. Fluid Mech.* **607**, 313–350.
- SCHMIDMAYER, K., BRYNGELSON, S. & COLONIUS, T. 2020 An assessment of multicomponent flow models and interface capturing schemes for spherical bubble dynamics. *J. Comput. Phys.* **402**, 109080.

- SHAMS, A., BIDI, S. & GAVAISES, M. 2023 Investigation of the ultrasound-induced collapse of air bubbles near soft materials. *Ultrason. Sonochem.* **102**, 106723.
- STRANG, G. 1968 On the construction and comparison of difference schemes. *SIAM J. Numer. Anal.* **5**, 506–517.
- VALKOV, B., RYCROFT, C. & KAMRIN, K. 2015 Eulerian method for multiphase interactions of soft solid bodies in fluids. *J. Appl. Mech.* **82**, 041011.
- YANG, J., RUBINO, V., MA, Z., TAO, J., YIN, Y., MCGHEE, A., PAN, W. & FRANCK, C. 2022 SpatioTemporally Adaptive Quadtree mesh (STAQ) Digital Image Correlation for resolving large deformations around complex geometries and discontinuities. *Exp. Mech.* **62**, 1191–1215.